Ocean Modelling 104 (2016) 28–44

Contents lists available at ScienceDirect

Ocean Modelling

journal homepage: www.elsevier.com/locate/ocemod

A multi-column vertical mixing scheme to parameterize the heterogeneity of oceanic conditions under sea ice

Antoine Barthélemy[a,*], Thierry Fichefet[a], Hugues Goosse[a], Gurvan Madec[b,c]

[a] Georges Lemaître Centre for Earth and Climate Research (TECLIM), Earth and Life Institute, Université catholique de Louvain, Louvain-la-Neuve, Belgium
[b] LOCEAN-IPSL, Sorbonne Universités, (UPMC Paris 6), CNRS/IRD/MNHN, Paris, France
[c] National Oceanography Centre, Southampton, United Kingdom

ARTICLE INFO

Article history:
Received 28 January 2016
Revised 16 May 2016
Accepted 21 May 2016
Available online 24 May 2016

Keywords:
Model
Ice thickness distribution
Subgrid-scale
Ocean vertical mixing
Arctic
Antarctic

ABSTRACT

The heterogeneity of ocean surface conditions associated with a spatially variable sea ice cover needs to be represented in models in order to represent adequately mixed layer processes and the upper ocean density structure. This study assesses the sensitivity of the ocean-sea ice model NEMO-LIM to a subgrid-scale representation of ice-ocean interactions. The sea ice component includes an ice thickness distribution, which provides heterogeneous surface buoyancy fluxes and stresses. A multi-column ocean scheme is developed to take them explicitly into account, by computing convection and turbulent vertical mixing separately in the open water/lead fraction of grid cells and below each ice thickness category. For the first time in a three-dimensional simulation, the distinct temperature and salinity profiles of the ocean columns are allowed to be maintained over several time steps. It is shown that the model response is highly sensitive to the homogenization time scale between the columns. If the latter are laterally mixed with time scales shorter than 10 h, subgrid-scale effects exist but the mean state is practically unaffected. For longer mixing time scales, in both hemispheres, the main impacts are reductions in under-ice mean mixed layer depths and in the summer melt of sea ice, following decreased oceanic heat flux at the ice base. Large changes in the open water temperature in summer suggest that the scheme could trigger important feedback processes in coupled simulations.

1. Introduction

The sea ice covering the surface of polar oceans is an extremely heterogeneous medium. Within a restricted region, areas of open water, thin newly-formed ice, level ice a few meters thick or pressure ridges several meters thick may be found (Thorndike et al., 1975). Because the insulating properties of ice strongly depend on its thickness, the atmosphere-ice-ocean interactions are highly spatially variable as well. The ice growth rate, which is associated with brine rejection in the underlying ocean, decreases rapidly with thickness, especially for thin ice (Maykut, 1982). Furthermore, warming of the oceanic mixed layer in summer results mostly from the absorption of solar radiation in ice-free areas (Maykut and McPhee, 1995). The effects of sea ice on the sea surface temperature and salinity, hence on upper ocean stratification and mixing, are therefore variable at small horizontal scales. The mixed layer dynamics, on the other hand, is of crucial importance for the evolution of the sea ice cover. Indeed, it determines the ice bottom boundary conditions, most importantly influencing the ice energy balance through modulations of the oceanic heat flux at the ice base.

Modeling studies have shown that representing the heterogeneous nature of ocean surface boundary conditions under sea ice might be necessary to achieve an adequate simulation of the upper ocean physics in polar regions (Losch et al., 2006). Convective mixing related to intense brine rejections following ice formation is for instance likely to prevail only in open water or thin ice areas, which may represent a small fraction of grid cells in large-scale models. Brine rejection parameterizations have been developed to mimic such processes (e.g., Nguyen et al., 2009), but their effect is to suppress convection instead of making it localized (Barthélemy et al., 2015). They are consequently not able to account for the entrainment of water from the upper pycnocline, which could constitute a significant component of the mixed layer heat budget (e.g.,

* Corresponding author. Georges Lemaître Centre for Earth and Climate Research, place Louis Pasteur 3, box L4.03.08, 1348 Louvain-la-Neuve, Belgium.

E-mail addresses: antoine.barthelemy@uclouvain.be (A. Barthélemy), thierry.fichefet@uclouvain.be (T. Fichefet), hugues.goosse@uclouvain.be (H. Goosse), gm@locean-ipsl.upmc.fr (G. Madec).

http://dx.doi.org/10.1016/j.ocemod.2016.05.005
1463-5003/

Polyakov et al., 2013; Close and Goosse, 2013). In the Arctic, a part of the solar heat that is absorbed in summer is indeed stored in a near-surface temperature maximum below the mixed layer (e.g., Jackson et al., 2012; Timmermans, 2015). In addition, although they are largely insulated from the surface layer by the strong halocline stratification (e.g., Toole et al., 2010; Shaw and Stanton, 2014), warm waters of Atlantic and Pacific origins are present at depth in the Arctic Ocean. Because of the much weaker stratification, entrainment of heat from below the mixed layer by localized convective mixing might be even more important in the Southern Ocean (e.g., Gordon and Huber, 1984; Martinson, 1990; Wong and Riser, 2011).

In most advanced sea ice models nowadays, an ice thickness distribution is used to represent the subgrid-scale variability of ice thickness, which has long proven crucial to simulate accurately the ice cover evolution (e.g., Hibler, 1980). Heterogeneous ocean surface boundary conditions are therefore available in such models. For example, in the coupled ocean-sea ice model NEMO-LIM (see the next section for description), all surface variables behave very differently in the open water fraction of grid cells compared to the ice-covered one (Barthélemy et al., 2016). This includes freshwater, salt, solar heat and non-solar heat fluxes and the surface stress. Salt and freshwater fluxes, as well as the solar heat flux reaching the under-ice interface in the Arctic, further show a strong dependency on ice thickness. However, the coupling with a single ocean grid cell underneath requires the subgrid contributions from the various fractions of the surface to be aggregated (Fig. 1). The information about their heterogeneity is hence not utilized and potentially important subgrid-scale ocean physics is not resolved. Such merging of subgrid-scale fluxes amounts to assuming an instantaneous lateral mixing between the different parts of the ocean model columns. Although horizontal homogenization definitely occurs, it is most likely not instantaneous in all situations. For instance, measurements performed during the SHEBA campaign (Surface Heat Budget of the Arctic Ocean) have shown that, following a period of calm winds, the surface of a lead had warmed to around 1 °C above the freezing point and freshened to become close to 15 PSU (Holland, 2003).

Previous studies have investigated the implications of explicit subgrid-scale vertical mixing schemes on ocean and sea ice simulations. By performing the mixed layer calculations separately in six columns corresponding to five ice thickness categories and to open water, Holland (2003) reproduced in a one-dimensional ocean and sea ice model the above-mentioned warming and freshening of summertime leads observed during SHEBA. In this study, the ice-covered columns were laterally mixed every time step, while the mixing with the open water column occurred every six hours. A large sensitivity to this homogenization time scale was underlined. Jin et al. (2015) implemented a two-column vertical mixing scheme in an ocean-sea ice configuration of the Community Earth System Model (CESM). The total salt flux resulting from ice growth was applied solely in one of the two columns, and lateral mixing between them occurred at the end of each time step. They noted strong effects on the simulated mixed layer depths only when the salt column was reduced to a size much smaller than the actual lead fraction. In the different context of heterogeneous ocean convection related to unresolved eddies, Ilıcak et al. (2014) also developed a two-column scheme with a homogenization at each time step. In contrast to the previous examples, changes in the depth of convective mixing between the columns were not caused by heterogeneous surface fluxes, but rather by different initial stratifications in each of them. Strong assumptions were needed to set the relative size of the two columns as well as the imposed spread in density profiles.

Our main objective in this study is to assess the impacts of a representation of subgrid-scale ice-ocean interactions on the NEMO-LIM model results. For that purpose, an improved multi-column ocean mixing scheme has been developed for NEMO-LIM, based on and generalizing the studies described above. The basic principle is to divide each ocean grid cell in several columns, whose areas are imposed by the ice thickness distribution and the open water fraction provided by the sea ice model. Those columns are forced at the surface by available subgrid fluxes and vertical physics computations are done separately in each of them (Fig. 1). The major novelty lies in the possibility to maintain different columns properties over several time steps. It is the first time that this option is enabled in three-dimensional simulations. The sensitivity to the columns' homogenization time

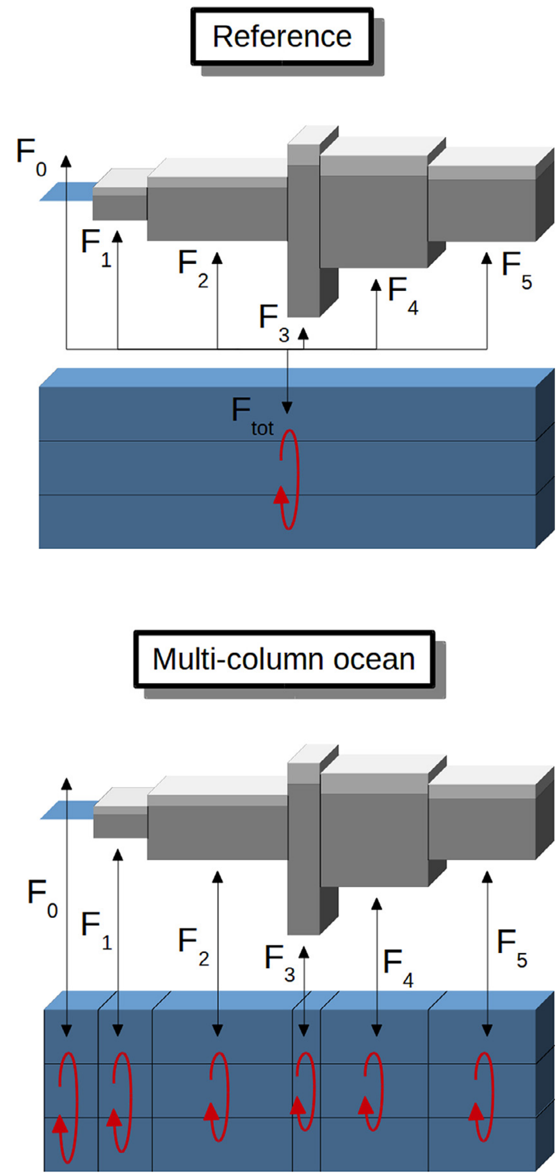

Fig. 1. Schematic illustration of the main principles of a multi-column ocean scheme. In the reference case, the subgrid fluxes and stress (F_n) from the sea ice model are aggregated before being transmitted to the single ocean grid cell underneath, and the ocean vertical physics computation (represented by a red arrow) is unique. In the multi-column case, the water column is divided into several sub-columns, corresponding to the open water fraction and to the categories of the ice thickness distribution. The specific fluxes and stress are applied at the surface of the sub-columns and the oceanic vertical physics is computed separately in each of them. (For interpretation of the references to color in this figure legend, the reader is referred to the web version of this article.)

scale is evaluated, and model results are analyzed in both polar regions.

This paper is organized as follows. The NEMO-LIM model setup and the multi-column ocean scheme are described in Sections 2 and 3, respectively. Results are presented and discussed in Section 4, starting with the heterogeneity of ocean surface boundary conditions in the reference simulation and continuing with the ocean and sea ice changes in the sensitivity experiments. A summary of our findings and concluding remarks are finally given in Section 5.

2. Model description

The current study is based on the global ocean-sea ice model NEMO-LIM, configured strictly in the same manner as in Barthélemy et al. (2016). Only the major model features and configuration aspects are thus described here, while components of importance to the multi-column scheme are presented in Section 3.2. A revised version of the Louvain-la-Neuve sea Ice Model (LIM3.6, Vancoppenolle et al., 2009; Rousset et al., 2015) has been incorporated in version 3.5 of NEMO (Nucleus for European Modelling of the Ocean, Madec, 2008). The ocean component is a finite difference, hydrostatic, free surface, primitive equation model, while LIM is a dynamic-thermodynamic sea ice model including an ice thickness distribution (ITD) and an advanced halodynamics scheme. The number of ice thickness categories N_{cat} is taken equal to five, with upper bounds for the first four categories fixed at 0.63 m, 1.33 m, 2.25 m and 3.84 m.

The reference model simulation is initialized in January 1948 with climatological temperature and salinity data from the World Ocean Atlas 2001 (Conkright et al., 2002) and is run until December 2014. The ocean-sea ice coupled model is forced using the so-called CLIO formulation, by a combination of NCEP/NCAR daily air temperature and wind reanalysis data (Kalnay et al., 1996) and of monthly climatologies for relative humidity, cloudiness, precipitation and river runoffs. The ice-ocean coupling is thoroughly discussed in Barthélemy et al. (2016), while surface heat fluxes are parameterized as in Goosse (1997). The sea surface salinity (SSS) restoring has a time scale of 310 days for a 50 m mixed layer, but it is reduced under sea ice, proportionally to the ice concentration, in order to avoid altering the ice-ocean interactions. The ocean and sea ice models share the quasi-isotropic global tripolar grid ORCA1, with a nominal 1° resolution in the zonal direction and 46 layers based on a z coordinate on the vertical, ranging from 6 m at the surface to 250 m at the bottom. The ocean model time step Δt is 1 h. LIM is embedded in the surface boundary condition (SBC) module of NEMO, which is called every six time steps.

While the model skill in representing the ocean will be addressed when we examine the sensitivity experiments results, a few comments about the sea ice simulation are worthy. In the reference configuration, LIM tends to overestimate the sea ice extent compared to observations (Barthélemy et al., 2016). The bias in the Arctic ranges between 1 and 2×10^6 km^2 throughout the year. In the Antarctic, the issue is most striking during the melting season, at the end of which the simulated extent is more than twice the observed one. The sea ice trends over the past decades, however, agree well in both hemispheres with satellite products (for the extent, Comiso, 2000) and reanalysis estimates (for the volume, Schweiger et al., 2011; Massonnet et al., 2013). NEMO-LIM is an appropriate tool to study the effects of a subgrid-scale representation of ice-ocean interactions, but this discrepancy between simulated and observed sea ice extents has to be kept in mind when analyzing model results.

Table 1
List of symbols used in the text.

Symbol	Description	Value and/or unit
Δt	Ocean time step	1 h
N_{cat}	Number of ice categories	5
N_{col}	Number of ocean columns	6
F_{fw}	Freshwater flux	kg m^{-2} s^{-1}
F_s	Salt flux	kg PSU m^{-2} s^{-1}
F_{sol}	Solar heat flux	W m^{-2}
F_{nsol}	Non-solar heat flux	W m^{-2}
F_b	Buoyancy flux	m^2 s^{-3}
τ	Norm of the surface stress	N m^{-2}
N^2	Square of the Brunt-Väisälä frequency	s^{-2}
K_z	Vertical eddy diffusivity	m^2 s^{-1}
$f^{(n)}$	Fractional area of column n	–
f_{mix}	Mixing fraction in MCO#2	–
τ_{hom}	Homogenization time scale in MCO#2	h

3. Multi-column ocean scheme

Our aim in this study is to develop a scheme in which the ocean vertical physics is calculated separately below the open water and the N_{cat} ice thickness categories, in order to investigate the role of subgrid-scale ice-ocean interactions. The ocean grid cells are therefore split into N_{col} parts that we name columns (with $N_{col} = N_{cat} + 1 = 6$), and the scheme is referred to as multi-column ocean (MCO). In this section, we first detail the modifications that are needed in the SBC module. Some background about the other ocean model components involved in the scheme is then presented, before describing the two distinct versions of MCO that will be tested. A list of symbols used in the text is provided in Table 1.

3.1. Surface boundary conditions

First of all, the MCO scheme requires keeping track of the SBC variables for each column separately. We follow exactly the methodology presented in Barthélemy et al. (2016), where additional details can be found. The code modifications are straightforward and simply consist in saving the contributions of open water and ice categories when they are calculated. They mostly take place in the sea ice code. The salt, freshwater, solar heat and non-solar heat fluxes are diagnosed for each column, as well as the norm of the surface stress. The latter is however identical for all ice categories. Since NEMO is used here in a linear free surface configuration, freshwater fluxes are turned into virtual salt fluxes that, along with real salt fluxes from sea ice processes, affect the SSS evolution.

A second modification is needed in the SBC and ice modules to allow the use of sea surface temperatures (SSTs) and SSSs specific to each oceanic column, instead of grid cell-average values. This further implies that the oceanic heat flux at the ice base can vary from one category to the other, mostly because of SST differences, but also because the ice bottom is at the local freezing point, which depends on the SSS.

3.2. Overview of relevant ocean model components

The MCO scheme requires substantial changes in the ocean model. The components of the code that are involved in its implementation are reviewed in Fig. 2. These are essentially the ones computing the vertical mixing and the update of tracers. Other components, related in particular to ocean dynamics and lateral mixing, are left untouched. Those only see the mean temperature and salinity (T/S) fields and are not directly affected by MCO.

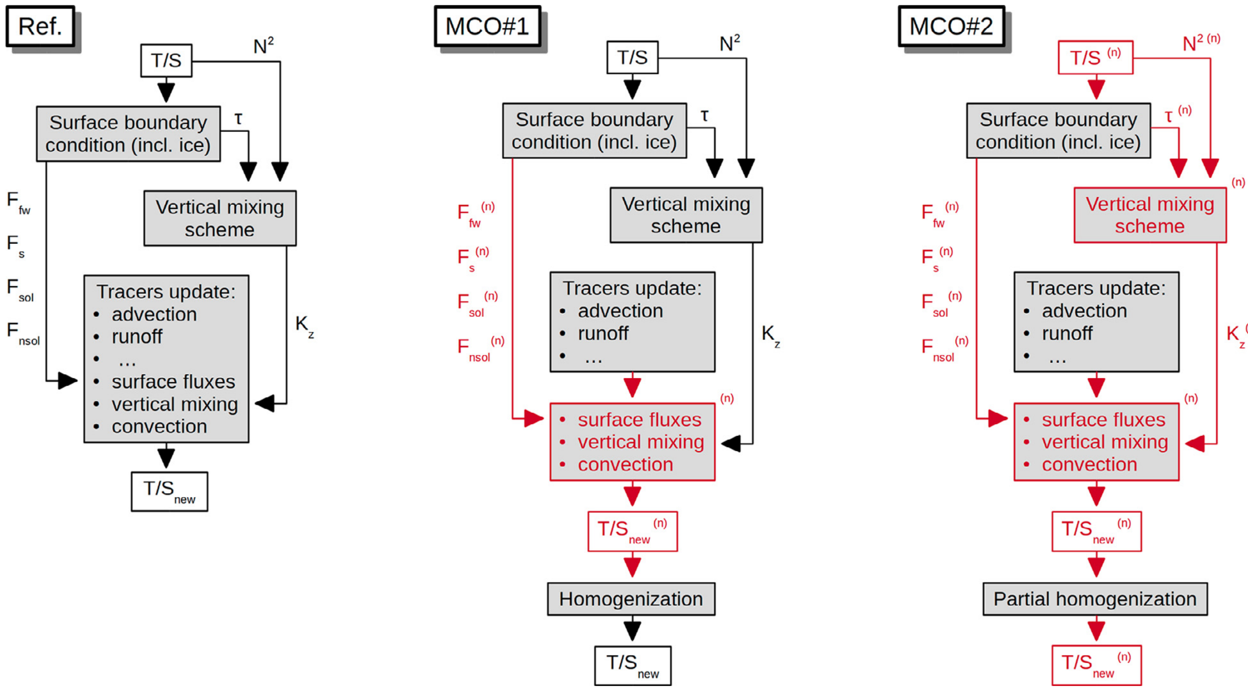

Fig. 2. Model components and variables relevant to MCO, as they stand in the reference code (left) and as they are modified in the MCO schemes (center and right). T/S denotes the temperature and salinity fields, whose surface values are used by the SBC module, while vertical profiles are used to compute the water column stability. Vertical mixing and convection are treated using the TKE and NPC schemes, respectively, which are described in Section 3.2. The elements in red and with exponents (n) are the ones that exist/are computed separately in each column. (For interpretation of the references to color in this figure legend, the reader is referred to the web version of this article.)

In our model configuration, turbulent vertical mixing is handled with the so-called TKE scheme (Blanke and Delecluse, 1993; Madec, 2008). Turbulent kinetic energy (TKE) is calculated from a prognostic equation. The vertical eddy viscosity and diffusivity are then derived using diagnostic non-local turbulent length scales. The TKE input at the surface is prescribed as a function of the norm of the surface stress τ, provided by the SBC module. Within the ocean, TKE is produced by vertical shear and destroyed by stratification, which is represented by the square of the Brunt-Väisälä frequency N^2. The TKE evolution is further influenced by vertical diffusion and Kolmogorov dissipation. Among the outputs of the TKE scheme, the most important one in the context of MCO is the vertical eddy diffusivity K_z.

The part of the code most impacted by MCO is the tracer update, where the changes in temperature and salinity from various processes are successively taken into account. Advection, lateral mixing, runoffs and bottom boundary layer processes are associated with tracer trends that will remain common to all columns. These trends are calculated using the mean T/S fields, without being affected by the subgrid-scale distribution of the tracers. Trends related to other processes will be computed separately in each column within the MCO schemes. These first include the application of surface fluxes (freshwater F_{fw}, salt F_s and non-solar heat F_{nsol}). The penetrative solar radiation scheme used in our configuration implies that the solar heat flux F_{sol} is not, strictly speaking, a surface flux. Instead, it is exponentially absorbed in the first few tens of meters of the ocean. We will nonetheless not make the distinction further in the text. The effect of vertical mixing is then calculated, using the K_z mixing coefficient from TKE. Finally, a non-penetrative convection scheme (NPC, Madec et al., 1991) is applied to remove the static instabilities that may have appeared in any of the ocean columns.

3.3. MCO#1

The main feature of the first version of the MCO scheme is to homogenize the oceanic columns at the end of each time step. It follows in this respect the work of Ilıcak et al. (2014) and Jin et al. (2015). Given the NEMO time-stepping, the only differences in turbulent mixing that could arise across the columns would be due to different surface stresses in open water/leads and below ice categories. However, Barthélemy et al. (2016) have shown that the stress is the SBC variable that shows the least variability at the subgrid scale. Therefore, in MCO#1, the only mixing process that is computed separately in each column is convection, which may present a strong heterogeneity as a result of the large subgrid-scale variability of buoyancy fluxes.

The details of the implementation are illustrated in Fig. 2. The tracer trends due to processes common to all columns are first calculated. These trends are then updated in the N_{col} columns using the specific thermohaline fluxes provided for each of them by the SBC module. In contrast to the study of Jin et al. (2015), where only a subgrid-scale repartition of salt fluxes is accounted for, we deal with all surface fluxes and with their simulated distribution across the open water/leads and ice categories. Vertical mixing is then computed, using however the same diffusivity K_z in each column. Finally, the NPC convection scheme is called, yielding N_{col} T/S profiles at each grid point. The last step consists in the homogenization of these profiles, which is done in a conservative way by weighting them by the columns relative areas.

3.4. MCO#2

The principle of the second version of MCO is to allow the ocean columns to be maintained over multiple time steps. In several aspects, it corresponds to a three-dimensional generalization of the study by Holland (2003). A number of technical issues need to be addressed and consequently make the implementation of MCO#2 much more complex than MCO#1. Furthermore, since the differences in T/S fields among the columns can grow over time, the vertical mixing scheme now also has to be called independently in each of them.

At the beginning of a time step, N_{col} T/S profiles are available at each grid point. The SBC module, including the sea ice model, receives SSTs and SSSs that may differ across the columns. This means in particular that atmosphere-ocean exchanges in open water are calculated with a specific SST. The heat fluxes at the base of each ice category are likewise computed with distinct SSTs and SSSs (hence freezing points).

The sea ice integration is possibly associated with shifts in the ITD and changes in the open water fraction, which induce modifications of the column areas. As a consequence, a redistribution of T/S profiles is required. It is handled in the following basic way. On the one hand, the properties of columns of decreasing area are unchanged. On the other hand, expanding ones are updated according to:

$$X_{new}^{(n)} = \frac{f_{old}^{(n)} X_{old}^{(n)} + (f_{new}^{(n)} - f_{old}^{(n)}) X_{rds}}{f_{new}^{(n)}},$$

where $X^{(n)}$ is the field considered and $f^{(n)}$ the fractional area of column n. The field X_{rds} used in the redistribution corresponds to the average in the areas lost by the decreasing columns:

$$X_{rds} = \frac{\sum_{n=1}^{N_{col}} \max(0, f_{old}^{(n)} - f_{new}^{(n)}) X_{old}^{(n)}}{\sum_{n=1}^{N_{col}} \max(0, f_{old}^{(n)} - f_{new}^{(n)})}.$$

By construction, this redistribution process is conservative and keeps the mean ocean properties unaltered.

In the vertical mixing scheme, the production of TKE by shear is computed only once, using velocities and a turbulent viscosity that are common to all columns. This term is then used in the TKE evolution calculations that are done separately in each column. These use distinct surface stress norms as boundary conditions in the ice-free and ice-covered parts of grid cells, as well as stratifications specific to each column. The subgrid-scale buoyancy fluxes are taken into account through this stratification term. The result is N_{col} vertical diffusivity profiles K_z at each grid point. The profiles of TKE by column are transferred to the next time step in exactly the same way as the T/S fields. They undergo in particular the same redistribution as described above. A final TKE computation is done based on the mean surface stress and mean stratification, in order to calculate the eddy viscosity for use in the ocean dynamics and in the shear production.

The update of tracers is basically the same as in the MCO#1 case, except that the turbulent vertical mixing coefficients can now differ among the columns. Nonetheless, a major difference is that the T/S profiles are only partially homogenized. More precisely, at each time step and for each oceanic column, a fraction f_{mix} of the profile is replaced by the average:

$$X_{new}^{(n)} = (1 - f_{mix}) X_{old}^{(n)} + f_{mix} X_{ave},$$

where the average X_{ave} is simply:

$$X_{ave} = \sum_{n=1}^{N_{col}} f^{(n)} X_{old}^{(n)}.$$

This partial homogenization intrinsically conserves the mean temperature and salinity. It actually corresponds to a restoring towards

Table 2
List of sensitivity experiments.

Experiment	MCO	f_{mix}	τ_{hom}
REF	no	n/a	n/a
S1.1	MCO#1	n/a	~ 1 h
S2.2	MCO#2	0.5	2 h
S2.10	MCO#2	0.1	10 h
S2.50	MCO#2	0.02	50 h
S2.250	MCO#2	0.004	250 h

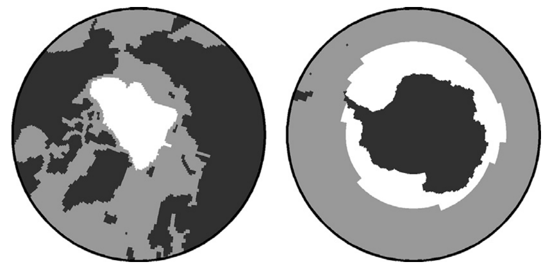

Fig. 3. Selected areas for the computation of spatial averages.

the mean profile, with a time scale τ_{hom} given by:

$$\tau_{hom} = \frac{\Delta t}{f_{mix}},$$

with Δt the ocean time step.

3.5. Sensitivity experiments

MCO#1 has no tunable parameter. The column homogenization in that version of the scheme is complete and has a fixed implicit time scale equal to the ocean time step, i.e. 1 h in our model configuration. The only parameter in the MCO#2 scheme is the homogenization time scale τ_{hom} between the columns. This lateral mixing is most likely variable both in space and time, because it depends on the columns distribution and on the ocean and sea ice dynamics (see the discussion in Section 4.4). For the sake of simplicity, it is kept constant within each of the simulations in this study.

The set of sensitivity experiments conducted in this paper is given in Table 2. The REF and S1.1 experiments correspond to the reference code without MCO scheme and to MCO#1, respectively. For MCO#2, a wide range of homogenization time scales are tested, from 2 to 250 h, which are equivalent to mixing fractions from 0.5 to 0.004. All sensitivity tests begin in 1985 from a restart of the REF simulation. They are run until end of 2014 and, unless otherwise stated, their last 20 year outputs are analyzed. The 10 year spinup is sufficient for the mixed layer and sea ice to adjust to the introduction of the MCO schemes. Short additional simulations have been performed with a higher coupling frequency between the sea ice and the ocean. The qualitative response to MCO remains the same as in the experiments presented hereafter, in which the coupling occurs every six ocean model time steps.

4. Results and discussion

The results of the reference and sensitivity experiments are now presented. We first illustrate the heterogeneity of SBC across the columns, then examine the impacts of MCO on the ocean properties and finally investigate feedbacks on the sea ice itself. Several diagnostics consist of spatial averages, which are computed in the areas represented in Fig. 3. The objective is to obtain mean val-

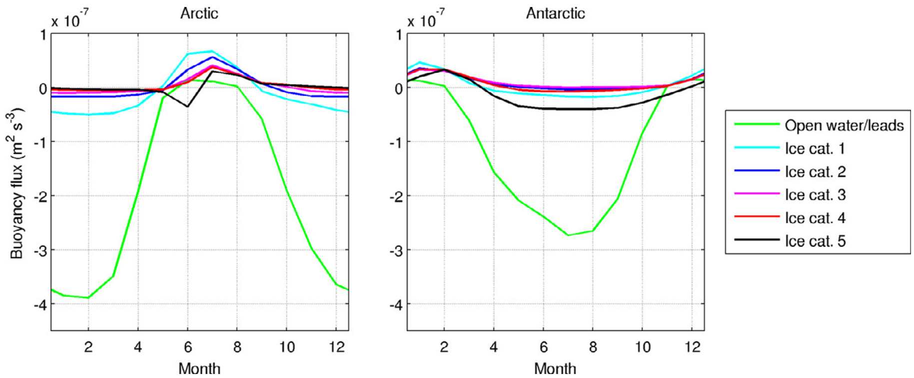

Fig. 4. Seasonal cycles of the ocean surface buoyancy flux in each column in experiment REF, averaged in the areas depicted in Fig. 3 and where sea ice concentration exceeds 15 %, in the Arctic (left) and in the Antarctic (right).

ues that are representative of the inner sea ice pack and of regions where significant changes occur in the ocean. The area chosen for the Arctic is delineated by the 500 m isobath and by the 80°N parallel in Fram Strait, hence excluding the highly stratified continental shelves where little vertical mixing occurs. Without an obvious physical northern boundary, the Antarctic area is based on a visual examination of the simulated sea ice concentration, and is chosen to ensure that it is fully covered with ice in winter.

4.1. Surface boundary conditions

A complete discussion of the modeled SBC heterogeneity across the columns in NEMO-LIM is provided in Barthélemy et al. (2016). Only major results are recalled here.

Changes in the density structure of the ocean upper layer, which may lead to convective mixing, are largely driven by the fluxes of salt, freshwater and heat that influence the evolution of SST and SSS. These fluxes can be combined into a single buoyancy flux F_b following:

$$F_b = \frac{g}{\rho_w}\left(\frac{\alpha_T}{c_w}(F_{sol} + F_{nsol}) - \beta_S F_s^*\right)$$

where g, ρ_w and c_w are the gravitational acceleration (9.81 m s^{-2}), reference seawater density (1035 kg m^{-3}) and specific heat (4000 J kg^{-1} K^{-1}), respectively. The thermal expansion and haline contraction coefficients α_T and β_S are taken equal to 0.3 10^{-4} K^{-1} and 7.7 10^{-4} PSU^{-1}, respectively, which are typical values for the cold and fresh waters found in the polar oceans (Marshall and Plumb, 2007). Finally, F_s^* is the total salt flux made up of real components from sea ice processes (F_s) and virtual components associated with freshwater fluxes (F_{fw}).

The mean seasonal cycles of the simulated ocean surface buoyancy flux for all columns are plotted in Fig. 4. Positive values indicate a gain of buoyancy, leading to an increase in stratification. The averaging is computed without weighting the fluxes by the column fractional areas. Furthermore, it only takes into account regions where the sea ice concentration exceeds 15 %. This threshold is useful in order not to include low ice concentration areas where the fluxes depart significantly from their inner ice pack values.

The most obvious features in Fig. 4 are the strong seasonality and the stark contrast between the ice and open water/lead columns. Since at low temperature the seawater density is mostly determined by salinity, the buoyancy fluxes follow closely the seasonal cycles of salt fluxes. The intense ice formation rates in leads in winter lead to large buoyancy losses associated with brine rejections. These are at least one order of magnitude larger than below ice. In summer, the strong warming of open water by solar radiation yields positive buoyancy fluxes. These are however weaker than the fluxes existing under melting ice due to the freshwater input at the ocean surface. In the model, water from melting ice and snow does not reach the open waters, because ice lateral melt, runoff from the ice surface and flushing of freshwater produced by bottom melt into the leads are not implemented.

Differences among ice categories also exist. In winter, thin ice grows more rapidly and therefore produces larger destabilizing salt fluxes. In summer, it loses its thinner insulating snow cover earlier, hence melting more rapidly. In the Arctic, penetration of solar radiation through thin ice categories also plays a minor role in strengthening their positive buoyancy fluxes. The peculiar behavior of thickest ice categories in summer in the Arctic and in winter in the Antarctic is due to the porosity of ridges in LIM. This parameter is taken equal to 0.3, following the estimate of Leppäranta et al. (1995) derived from in situ observations. Large amounts of salty water are thus entrapped when thick ice forms through ridging, and the subsequent brine drainage gives rise to large salt fluxes below the thickest ice.

In LIM, the ocean-ice stress is the same for all ice categories. As shown in Barthélemy et al. (2016), the surface stress is characterized by a much weaker seasonality than the thermohaline fluxes, and does not differ much between the columns. Still, on average in the Arctic, it is up to twice as large in open water compared to ice. In the Antarctic on the other hand, the stress tends to be stronger below ice and differs by less than 15 % in the ice-free fraction of grid cells.

By influencing ocean and sea ice (see the next sections), the introduction of the MCO schemes implies feedbacks on the SBC variables, mostly on the thermohaline fluxes. It turns out that this results in only slight quantitative adjustments to the main picture described above, which remains fully valid. These are therefore considered second order effects that will only briefly be addressed in the context of sea ice changes induced by MCO.

4.2. Ocean

The impacts of MCO on the ocean are presented in this section. We consider first the subgrid-scale processes, and then examine what influence they have on the mean fields.

4.2.1. Subgrid-scale processes

The difference between the depth of convection (CVD) in each column and the mean mixed layer depth (MLD) in winter is shown in Fig. 5. As its name implies, the CVD is the depth up to which the ocean column is homogenized by the NPC algorithm in order to remove static instabilities. A single MLD value is computed at each grid point from the mean density profile. It is defined in the model as the depth where the density is 0.01 kg m^{-3} higher than in the second level, at 10 m depth. The CVD - MLD difference maps are shown for February in the Arctic and for August in the Antarctic. This is just before the sea ice maximum, at a time when sea ice still forms in all regions but the ice edge and when the spread between subgrid-scale fluxes is the largest. Experiments S1.1 and S2.50 are presented. This first one illustrates the effects of the MCO#1 scheme, while the second is used to exemplify a situation in which clear changes in the mean fields are obtained (see the next section).

In experiment S1.1, the deepest CVDs within the sea ice zone are close to the MLD, suggesting that convective mixing due to surface fluxes (mostly brine rejections) is a major process in the mixed layer deepening. Furthermore, a gradient in CVD exists among the columns, which is readily explained by the variability of ice growth rates, the latter being the most intense in leads and decreasing with increasing sea ice thickness. An exception is the fifth ice category in the Antarctic, whose concentration is nonetheless very low, due to brine drainage from ridges as explained above. The differences of CVD between the columns also occur because a finite, weak stratification may exist inside the mixed layer in the multi-column formalism. Indeed, whenever a single ice category melts, the mean profile resulting from the averaging of one stratified column with others, possibly undergoing convection, will present a weak stratification close to the surface. Only the most intense brine rejections will generate enough instability to overcome this stratification. Convection shallower than the MLD occurs in two other cases. First, in both hemispheres, the melting of ice advected towards warmer waters produces freshwater fluxes that inhibit convection, as is the case close to the ice edge. Second, in the Antarctic, the Ross and Weddell Seas are characterized by relatively small CVDs. In those regions, the very weak stratification at depth may however cause an overestimation of the MLD estimated using the density threshold method.

The MCO#2 scheme allows differences in temperature and in salinity between the columns to accumulate over several time steps. As a consequence, in experiment S2.50, convection is able to penetrate well below the mean MLD for the columns with the strongest surface fluxes. This includes in both hemispheres the column corresponding to leads, as well as the first (and to a lesser extent the second) sea ice category in the Arctic. The effect related to saline, newly formed ridges is again visible for the fifth category. In S2.50, north of Greenland and the Canadian Arctic Archipelago (CAA), convection in leads reaches depths more than 20 m larger than the mean MLD, while it can be up to 50 m in many coastal regions along Antarctica. Changes in MLDs compared to the reference experiment are smaller than these values (see Fig. 7). This means that the MCO#2 scheme allows, in at least a fraction of the grid cells, to entrain within the mixed layer waters from below, which would not have been put in contact with the surface otherwise.

The T/S profiles in each column are plotted in Fig. 6. Only experiment S2.50 is considered here, since such profiles exist exclusively in the MCO#2 scheme. Winter profiles are for the same months as in Fig. 5, while summer results are for July in the Northern Hemisphere (NH) and January in the Southern Hemisphere (SH), when the subgrid-scale fluxes are the most representative of the summer season.

The profile characteristics are fairly consistent for both hemispheres in each season. Expectedly, the most visible differences are between the open water/leads column and the ice ones. In winter, the column corresponding to leads is more saline in the mixed layer, by 0.25 PSU down to around 25 m in the Arctic and by 0.1 PSU down to 50 m in the Antarctic. This arises from additional salt input at the surface, as well as from entrainment of saltier water from below through deeper convection. A very slight salinity gradient also exists among ice categories in the NH. The effect of deeper convective mixing in leads has an impact on temperature profiles too. Vertical mixing of warmer water from below the mixed layer with cold surface water results in an increase (decrease) in temperature above (below) the MLD. Differences are nevertheless weak, of the order of 0.1 °C in the Antarctic and even smaller in the Arctic.

Summer profiles feature temperatures well above the freezing point in open water. The SST difference between open water and ice columns amounts on average to 1 °C in the NH and to 0.75 °C in the SH. This is caused by the absorption of around 150 W m^{-2} of solar energy in ice-free areas, only partly balanced by non-solar heat losses less than 20 W m^{-2} in the Arctic and less than 50 W m^{-2} in the Antarctic (Barthélemy et al., 2016). By contrast, the summer ocean-to-ice heat flux maintains the under-ice water close to the freezing point. Nevertheless, in the Arctic, the transmission of a fraction of incoming solar radiation through thin, snow-free ice leads to SST differences of up to a few tenths degrees between the thinnest and the thickest ice categories. This does not happen in the Antarctic, because ice remains covered with snow during summer, which absorbs all solar energy in the model.

Salinity profiles indicate that thin ice melts more rapidly, leading to a fresher ocean surface below the first categories. Differences are of the order of a few tenths PSU and are confined to the uppermost ocean levels. The highest SSSs are encountered in open water. This contrasts with the examination of SHEBA data by Holland (2003), which showed the surface of the lead to be several PSU fresher than the under-ice. Absence of explicit lateral melt and of meltwater runoff from the ice surface in LIM are likely to be responsible for this discrepancy.

An equivalent of Fig 5 for the summer season would show the same absence of convection in all columns. Fig. 6 indicates however that distinct situations occur in open water and below ice. On the one hand, melting ice has a cooling but freshening effect on the ocean surface. On the other hand, the open water undergoes little salinity changes from surface fluxes, but warms due to the absorption of solar radiation. In both cases, the water columns become stable and vertical mixing is hampered.

4.2.2. Effects on mean fields

In this section we determine whether MCO has an impact on the ocean mean state, beyond the subgrid-scale effects described above. MLDs could be affected in two ways. Firstly, the application of destabilizing surface fluxes in a limited part of the grid cells, and the fact that the average of unstratified and stratified profiles is stratified, could lead to a reduction in MLDs. Secondly, the deeper convection in some columns could weaken the stratification below the MLD compared to the reference experiment, which could permit a greater penetration of turbulent mixing and an increase in MLDs. As will be shown here and in agreement with previous studies (Ilıcak et al., 2014; Jin et al., 2015), the first effect is in general dominant in winter.

In the NH, the simulated MLDs are compared with the global upper ocean MIMOC climatology (Monthly Isopycnal and Mixed layer Ocean Climatology, Schmidtko et al., 2013). This product is based on individual conductivity-temperature-depth (CTD) profiles from traditional shipboard data, but also from automated ice-tethered profilers, which provide upper ocean observations of the

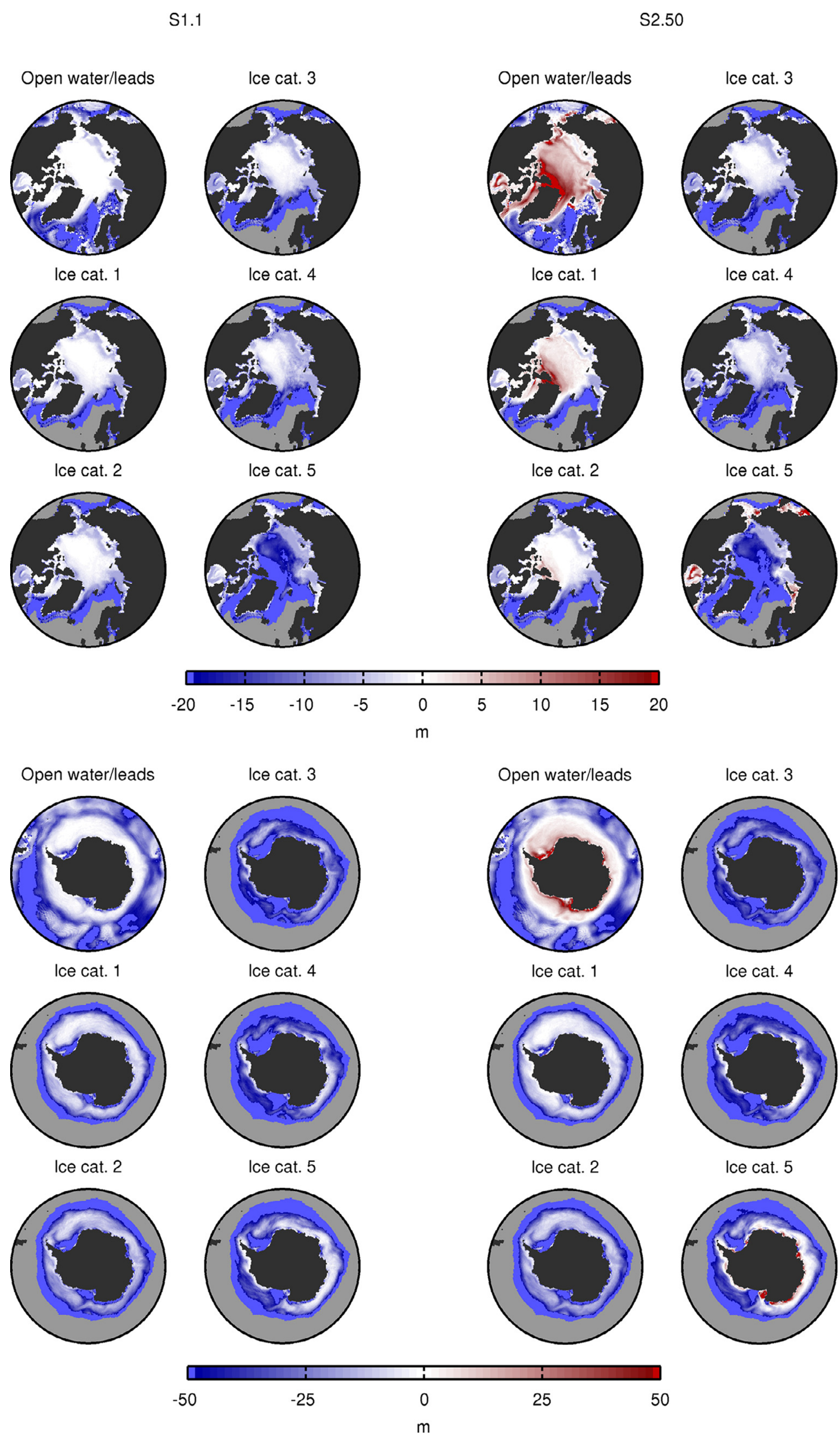

Fig. 5. Difference between the convection depth in each oceanic column and the mean mixed layer depth, in experiments S1.1 (left) and S2.50 (right), for February in the Arctic (upper panels) and for August in the Antarctic (lower panels).

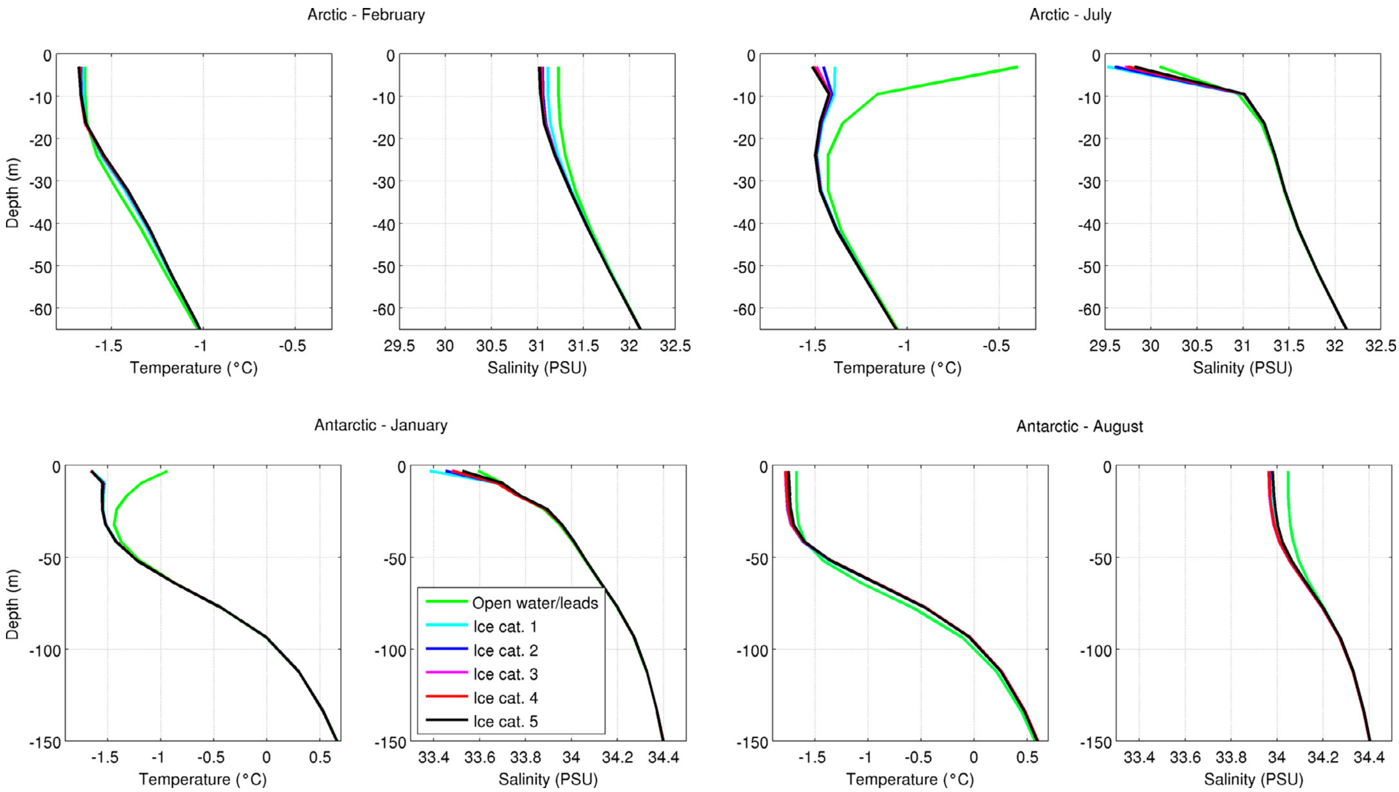

Fig. 6. Temperature and salinity profiles in each oceanic column in experiment S2.50, averaged in the areas depicted in Fig. 3 and where sea ice concentration exceeds 15 %, for February and July in the Arctic (upper panels) and for January and August in the Antarctic (lower panels).

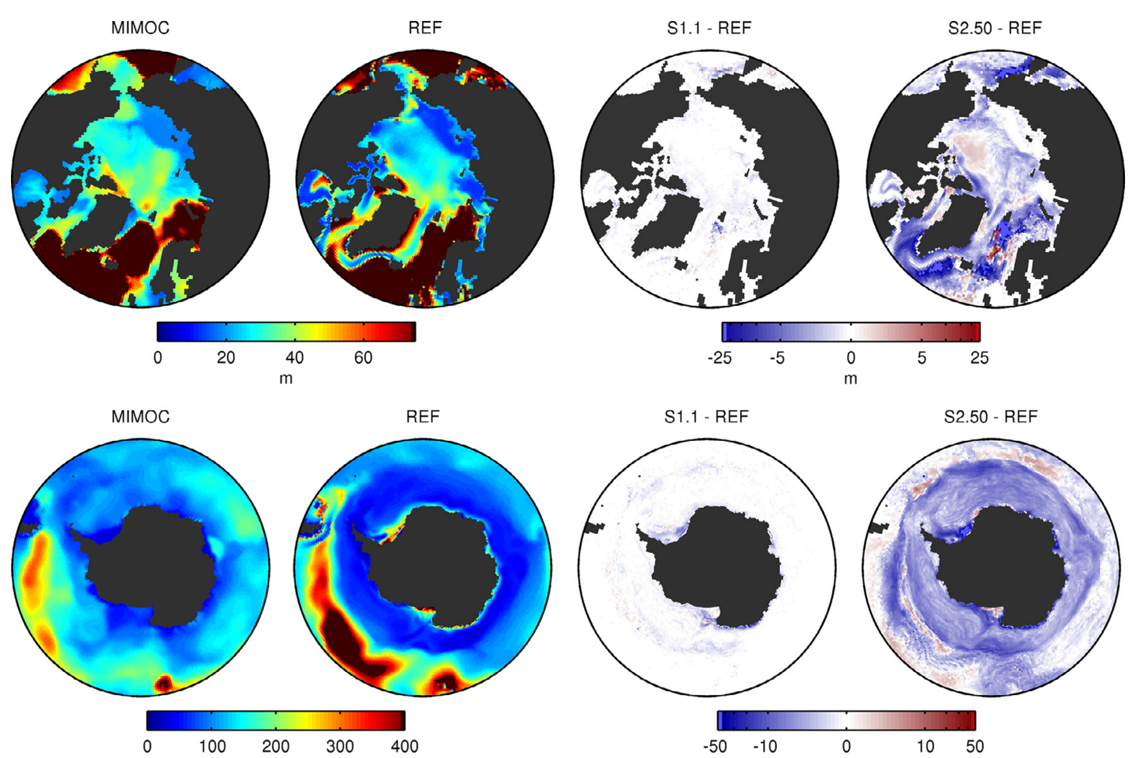

Fig. 7. Mixed layer depths in the MIMOC climatology and in experiment REF, and differences with experiments S1.1 and S2.50, for February in the Arctic (upper panels) and for August in the Antarctic (lower panels). A logarithmic color scale is used in the difference maps.

Table 3
Monthly maximum of the average mixed layer depth in the areas depicted in Fig. 3 and sea ice extent and volume monthly extrema, in the reference and sensitivity experiments, in the Arctic (upper part) and in the Antarctic (lower part). The numbers in brackets indicate the differences compared to the reference experiment.

Experiment	REF	S1.1	S2.2	S2.10	S2.50	S2.250
Arctic						
Max. MLD (m)	34	34 (0)	35 (1)	35 (1)	33 (-1)	29 (-5)
Min. extent (10^6 km^2)	7.0	7.0 (0.0)	7.0 (0.0)	7.2 (0.2)	7.7 (0.7)	8.5 (1.5)
Max. extent (10^6 km^2)	16.8	16.8 (0.0)	16.8 (0.0)	16.8 (0.0)	16.9 (0.1)	17.0 (0.2)
Min. volume (10^3 km^3)	14.7	14.7 (0.0)	14.8 (0.1)	15.2 (0.5)	16.8 (2.1)	19.3 (4.6)
Max. volume (10^3 km^3)	30.8	30.8 (0.0)	30.9 (0.1)	31.1 (0.3)	32.0 (1.2)	33.3 (2.5)
Antarctic						
Max. MLD (m)	79	78 (-1)	78 (-1)	76 (-3)	73 (-6)	69 (-10)
Min. extent (10^6 km^2)	8.0	8.0 (0.0)	8.1 (0.1)	8.4 (0.4)	9.6 (1.6)	11.4 (3.4)
Max. extent (10^6 km^2)	20.9	20.9 (0.0)	20.9 (0.0)	21.0 (0.1)	21.1 (0.2)	21.2 (0.3)
Min. volume (10^3 km^3)	5.6	5.6 (0.0)	5.6 (0.0)	5.8 (0.2)	6.6 (1.0)	7.6 (2.0)
Max. volume (10^3 km^3)	16.6	16.6 (0.0)	16.6 (0.0)	16.7 (0.1)	16.8 (0.2)	16.9 (0.3)

ice-covered Arctic region in all seasons (Krishfield et al., 2008). As shown in Fig. 7, experiment REF reproduces relatively well the MLDs in the Arctic Ocean in winter. The main biases compared to the climatology are too deep MLDs in areas around Greenland, in Hudson Bay and in the Sea of Okhotsk, and a slight underestimation of MLDs in the Canada Basin.

On average in the Arctic area chosen for analysis (Fig. 3), the maximum monthly MLD in MIMOC is 34 m. The corresponding values for all simulations are listed in Table 3. The good agreement with REF is noticeable. The mean impact of MCO is weak, except for simulation S2.250 which exhibits a maximum MLD reduction of 5 m. The small changes in that mean value could result from the spatial averaging, but as far as experiment S1.1 is concerned, Fig. 7 shows that MCO#1 has indeed nearly no impact. In S2.50 on the contrary, MLDs generally decrease in the sea ice zone, up to 10 m north of Greenland, but they show a weak increase in the Canada Basin. However, the changes are too small to offset the initial model biases. The largest differences actually occur beyond the sea ice edge, in regions of much deeper MLDs, likely because of weak modifications in the large-scale T/S fields.

Due to the lack of under-ice winter hydrographic observations close to Antarctica, the MIMOC climatology severely underestimates MLDs on the continental shelves (Barthélemy et al., 2015). Besides, measurements collected between 2004 and 2011 by CTD sensors carried by seals provide an extremely valuable source of information about the hydrography of the Southern Ocean south of the Antarctic Circumpolar Current. We thus use here the MEOP-CTD dataset (Marine Mammals Exploring the Oceans Pole to Pole, Roquet et al., 2011; 2013), a calibrated compilation of T/S profiles collected by hundreds of instrumented seals, to evaluate our model results. In short, climatological MLDs are obtained from the database by averaging, for each month and each ORCA1 grid point where they are available, the MLDs computed from the measured profiles in the same way as they are estimated in NEMO. More details about the model-data comparison can be found in Barthélemy et al. (2015). Out of the continental shelves, the MLDs from MIMOC compare quite well with the ones calculated from seal observations. Hence, the following analysis is only based on the latter.

MLDs in experiment REF are evaluated against MEOP-CTD estimates in Fig. 8. The map of differences is shown for the month of May, when mixed layers become deeper and when the data coverage is still relatively good. Overall, the model tends to underestimate MLDs. The issue is clearest along the coast of East Antarctica, where the bias is locally up to 150 m. The only location where significantly too deep mixed layers are modeled is the eastern Weddell Sea. The scatter plot extends the evaluation to all months and supports the above finding. Weddell Sea data points are clustered above the diagonal. The correlation between simulated and observed MLDs is 0.38 and the slope of the least square linear fit is 0.59, confirming the MLD underestimation by the reference experiment.

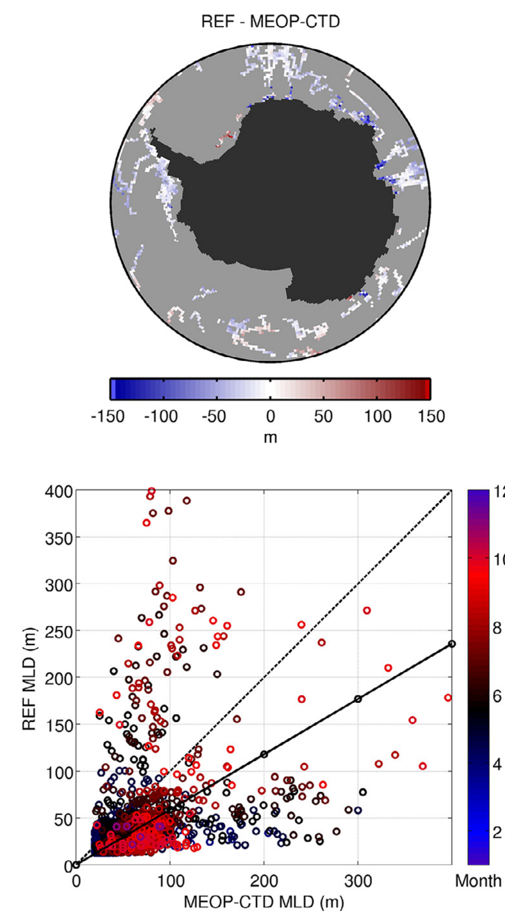

Fig. 8. Comparison of mixed layer depths in the MEOP-CTD dataset and in experiment REF, for the period 2004–2011. Upper panel: mixed layer depths difference in May. Lower panel: scatter plot of simulated versus observed mixed layers depths in the Antarctic area depicted in Fig. 3; the solid line is a least squares linear fit and the dashed line is the diagonal.

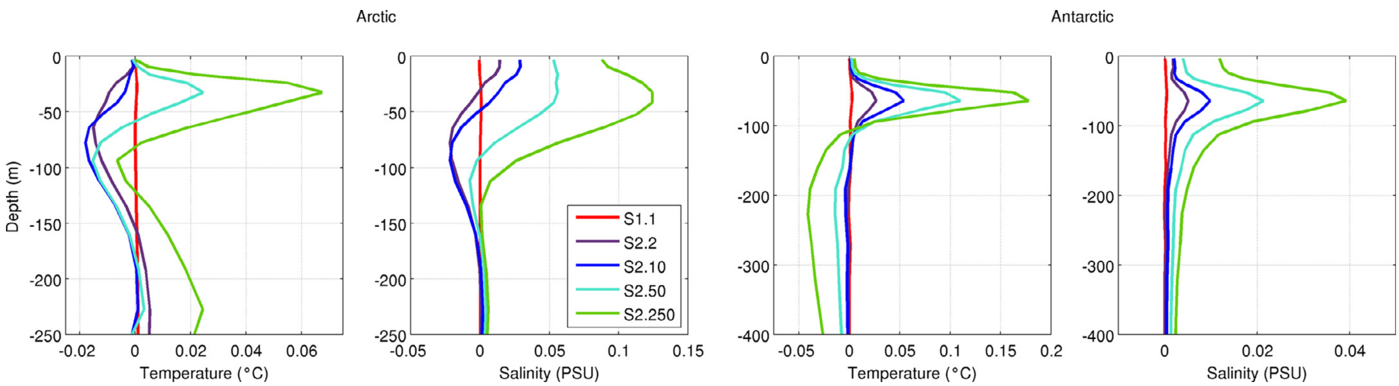

Fig. 9. Differences in temperature and salinity profiles between the sensitivity and REF experiments, averaged in the areas depicted in Fig. 3, for February in the Arctic (left) and for August in the Antarctic (right).

As in the NH, the introduction of MCO schemes in NEMO reduces MLDs in the Antarctic, with a larger impact for longer homogenization time scales. On average, the MLD drops from 79 m in REF to 73 m in S2.50 (Table 3), whereas the changes are barely visible for S1.1 (Fig. 7). Substantial decreases in MLD appear more restricted to the ice-covered areas than in the Arctic. The largest changes, of the order of 50 m in experiment S2.50, occur on the continental shelves, except in the Ross Sea. A comparison of S2.50 with the MEOP-CTD dataset yields a correlation coefficient of 0.41 and a linear fit slope of 0.54. This is consistent with a small improvement in the mean MLD representation where measurements exist in the Weddell Sea, but with an increased underestimation elsewhere. The equivalent of Fig. 8 for this experiment looks very similar to the one displayed for REF and is thus not shown. Since the MEOP-CTD profiles are recorded during the quasi-vertical ascent of seals, it is possible that the animals oversample the lead areas. Because of the large differences in the depth of convection between the columns in MCO#2, such a non-uniform sampling could have an influence on the model-observation comparison.

The MCO effects on mean T/S fields are presented in Fig. 9. They are negligible in S1.1 and small in all other simulations, so that the general shape and properties of profiles remain mostly unaffected. Therefore, the differences compared to the reference experiment are plotted for the winter season. In summer in both hemispheres, the most consistent signal is an increase in SSS (not shown) that we attribute to a reduced sea ice melt (see the next section). Profiles averaged over various sectors of the Southern Ocean present the same key features as described below.

In the Antarctic, the temperature and salinity increase at a depth close to the MLD, with a magnitude depending of the homogenization time scale. This is consistent with a shoaling of the mixed layer, which allows the warmer and saltier water from below to get closer to the surface. The maximum warming and salinity gain are of 0.1 °C and 0.02 PSU in experiment S2.50. The temperature profiles also indicate a slight cooling at depth, which is explained by a greater penetration of cold water due to deeper convection in leads. At the surface, the presence of sea ice forces temperatures to remain at the freezing point in all simulations.

In the Arctic, the model response does not seem linear as a function of the mixing time scale. For experiments S2.2 and S2.10, only a weak cooling is present down to 150 m. A warming in the upper layer, associated with a MLD shoaling or to the entrainment of water from below, exists exclusively in S2.50 and S2.250. The temperature differences at greater depths (below 150 m) likely originates from changes in vertical mixing in remote areas, with impacts on deep water masses. Certainly, the changes are minimal, being at maximum of the order of 0.02 °C in experiment S2.50, which is too small to correct the generally large temperature biases of current models at intermediate depths in the Arctic Ocean (e.g., Ilıcak et al., 2016). Salinity profiles show the same variety of behaviors, with a consistent increase close to the surface but with a freshening below the mixed layer only in S2.2 and S2.10.

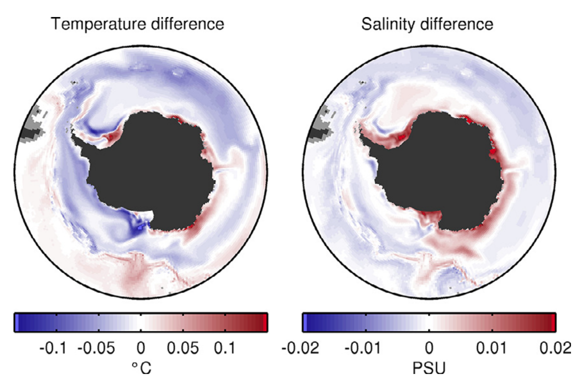

Fig. 10. Differences in temperature (left) and salinity (right) at 190 m depth between experiments S2.50 and REF, for August in the Antarctic.

The MCO impacts on mean T/S profiles are thus weak, especially for temperature in the Arctic and for salinity in the Antarctic. This may appear surprising in comparison to the subgrid-scale effects presented in the previous section. This is because some of the subgrid-scale processes occur in columns of very small extent. The most meaningful example is winter leads, whose vertical mixing and hydrography are so peculiar. Their average concentration in the model falls to less than 0.03 % in February in the Arctic and to less than 0.5 % in August in the Antarctic. A higher and more realistic simulated open water fraction would strengthen the effects of MCO, by increasing the area of the column with the strongest buoyancy fluxes and the deepest convection.

Additionally, the mean profiles considered so far mask regional changes that are larger in magnitude. Spatial distributions of temperature and salinity differences at 190 m depth between experiments S2.50 and REF are shown in Fig. 10 for August in the Antarctic. While changes close to the surface are relatively uniform (not shown), complicated patterns exist at this depth, because it is locally below, near or above the mixed layer base. The mean difference plotted in Fig. 9 is therefore not representative of all regions.

At depths greater than the MLD, however, the changes caused by MCO tend to be very small everywhere.

Especially in the Ross Sea, the cooling effect of MCO below the MLD is clear, reaching up to 0.15 °C for the waters exiting the continental shelf. In the Weddell Sea, higher temperatures are found close to the ice shelf where the mixed layer is deeper than 190 m, while colder waters occupy the other areas. This is consistent with the one-dimensional effect described above based on mean profiles. In absolute values, maximum differences are of the order of 0.15 °C as well. Along the coast of East Antarctica, waters at 190 m depth are warmer in S2.50 than in REF, which cannot always be explained by deep MLDs as in the Weddell Sea. At 1° resolution, we do not expect an accurate representation of the coastal currents. Nonetheless, changes in the zonal ocean velocity (not shown) are a possible reason for the different model response in that region. The salinity presents a more uniform increase along the continent, up to 0.02 PSU in the three areas discussed above.

The changes induced by MCO are robust, in the sense that the differences between the experiments are similar if we select other time intervals in the simulations. They are also non-negligible when put into perspective with observed decadal variations in the temperature of bottom water masses in the Weddell Sea for example, which occur at rates close to 0.01 °C year^{-1} (e.g., Fahrbach et al., 2004; Couldrey et al., 2013). Nevertheless, these changes are small compared to the model bias or to the variability of the system. Specifically, the application of a Student t-test has demonstrated that the changes in mean temperature and salinity are almost never statistically significant when compared to the interannual variability. At this depth around Antarctica, the simulated interannual standard deviation is indeed of the order of 0.3 °C for temperature and 0.05 PSU for salinity.

4.3. Sea ice

The impacts of the MCO schemes on the sea ice cover are now investigated. Maximum and minimum monthly ice extents and volumes are given for all sensitivity experiments in Table 3. The overall effect of MCO is to increase the ice extent and volume, mostly at the seasonal minimum. It is weak for homogenization time scale equal or shorter than 10 h, but becomes substantial for S2.50 and S2.250. In those simulations, the minimum sea ice extent rises by around 1 10^6 km^2 in the Arctic. The increase is even larger in the SH, but given the positive summer bias in Antarctic sea ice, the model results should be treated with caution. In both hemispheres, the extent is only marginally affected at the winter maximum. The Arctic sea ice volume changes are similarly at their highest during summer, reaching for instance 2.1 10^3 km^3 for experiment S2.50, but approximately half of the signal persists during winter. In the Antarctic, differences in volume occur mainly at the sea ice minimum and amount to 1.0 10^3 km^3 for S2.50.

Maps of sea ice concentration and thickness are shown in Fig. 11, for experiments REF and S2.50, which is the first in which MCO has significant effects, and for the months of February and August when the differences with respect to the reference simulation are the largest. It is worth noting that these months are not the ones corresponding to the simulated sea ice minimum (March and September), which could give an exaggerated impression of the real model bias in summertime ice extent. The average sea ice thickness over the whole grid cell is plotted, i.e. ice 1 m thick at 50 % concentration appears as 0.5 m thick in the figure. In other words, it corresponds to the sea ice volume per unit area.

Sea ice concentration increases preferentially in peripheral areas where it is low, whereas it is almost unchanged in the central Arctic basin and CAA, and in the Weddell Sea. Differences are typically of the order of 10 %, but exceed 15 % locally. The gains in ice thickness tend to be more widespread. In the Arctic, ice gets 15 cm thicker almost everywhere and the increase is up to 30 cm in the marginal ice zone. The thickening is at most 15 cm in the Antarctic. Although the magnitude of the changes varies from one sensitivity experiment to the other, the general patterns remain the same in all cases.

In order to understand the origin of the sea ice changes described so far, we examine the non-solar part of the oceanic surface heat flux in experiments REF and S2.50 (Fig. 12). In the ice-covered columns, this corresponds practically to the heat transferred from the ocean to the ice base. In current ocean-sea ice models, and in our reference simulation in particular, the oceanic heat flux is common to all ice categories. With MCO#2, it can vary from one category to another one, according to the specific ocean conditions underneath.

Considering first the subgrid-scale distribution in S2.50, Fig. 12 shows that the heat flux at the ice base tends to be larger for thinner ice. In the Antarctic, the differences are limited to the winter season and are of the order of 5 W m^{-2} between the first and the third and fourth categories, which is roughly 30 % in relative terms. The highest fluxes are caused by enhanced vertical mixing that brings more oceanic heat to the surface. With its large salt fluxes resulting from brine drainage, the fifth category behaves in a similar way as the first. The same processes occur in winter in the Arctic as well, where the heat flux below the thinnest ice is more than twice as high as below the thickest category. However, in contrast to the SH, the fluxes are also heterogeneous in summer. At the maximum in August, the first, the second and the other categories undergo fluxes of 27, 22 and around 20 W m^{-2}, respectively. This arises from differential penetration of solar radiation for the different ice classes. On average, a maximum difference of 15 W m^{-2} in the amount of energy reaching the ice-ocean interface indeed exists between the first two categories (Barthélemy et al., 2016). The lateral mixing between the columns and the penetration of shortwave radiation inside the ocean imply that only a third of this difference is reflected in the oceanic heat fluxes to the ice.

Comparing the oceanic heat fluxes between experiments REF and S2.50 is also of interest. During winter in both hemispheres, the REF curve tend to follow the S2.50 curve corresponding to the category in which most ice lies (third in the NH and second in the SH), suggesting modest differences between both simulations. In summer the signal is clear nonetheless: the fluxes in the MCO experiment are systematically lower than in the reference simulation. The difference is between 5 and 10 W m^{-2} in the Arctic on average, but reaches as much as 15 W m^{-2} in the Antarctic. The main source of heat to the ocean in summer is the warming by solar radiation, which is maximum in open water. Without an MCO scheme, the absorbed energy is immediately spread over the whole grid cell. When MCO#2 is activated, the warming is concentrated in the open water column. It reaches the under-ice only thanks to the column homogenization, which is controlled by the mixing parameter f_{mix}. This explains the lower ocean-to-ice heat fluxes, and consequently the reduced sea ice melt. This process also explains that the differences between MCO#2 and REF are the largest where concentration is low, because it is where the amount of solar energy entering the ocean is the highest.

Also shown in Fig. 12 are the non-solar heat fluxes at the surface of open water/leads. When sea ice forms, this is actually not the total heat loss to the atmosphere, but rather the flux needed to keep the ocean close to the freezing point. The additional term corresponding to the heat losses associated with the freezing of seawater has no impact on the SST. This is the reason why it is not included in this diagnostics. Focusing on the surface boundary

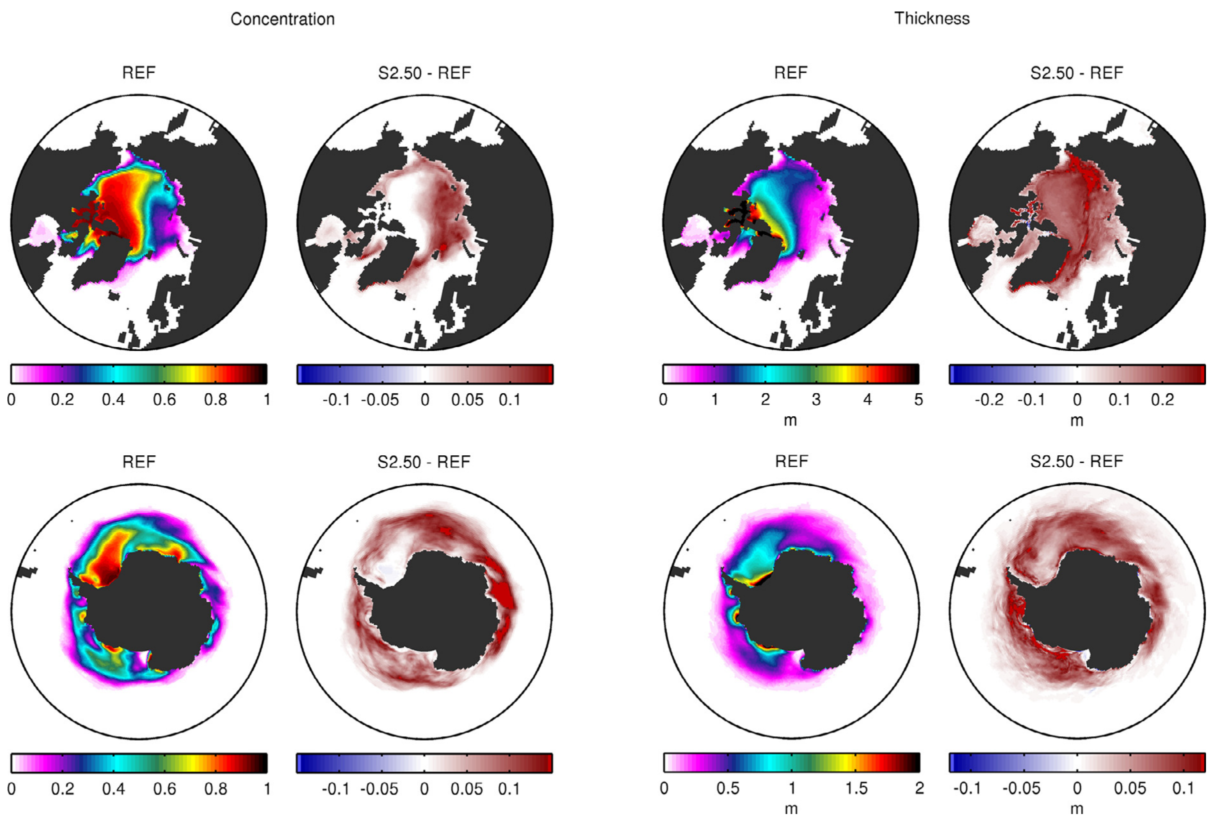

Fig. 11. Sea ice concentration (left) and mean thickness (right) in experiment REF, and differences with experiment S2.50, for August in the Arctic (upper panels) and for February in the Antarctic (lower panels).

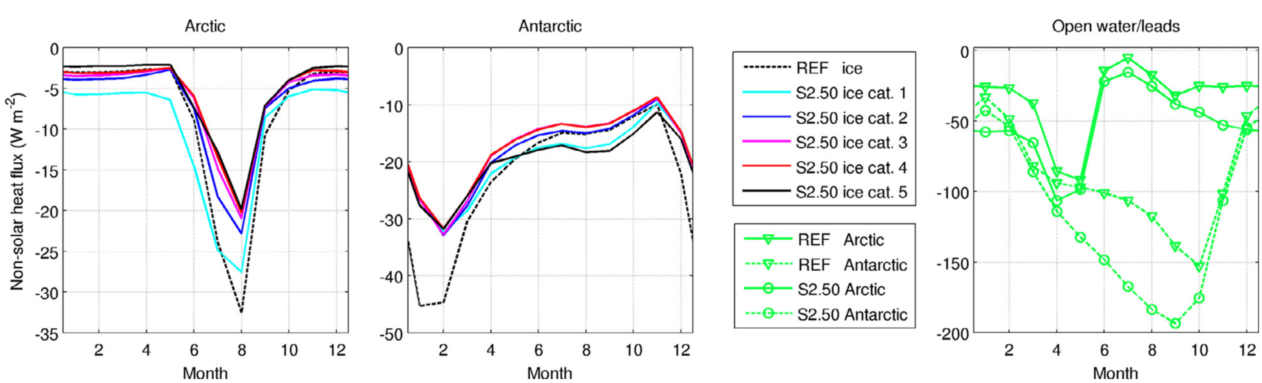

Fig. 12. Seasonal cycles of non-solar heat flux at the ocean surface under ice (left) and in open water/leads (right) in experiments REF and S2.50. The spatial averages are computed in the areas depicted in Fig. 3 and where sea ice concentration exceeds 15 %.

condition for the ocean, the changes between experiments with or without MCO are substantial. The heat losses are higher in winter because deeper convection in leads brings more heat to the surface and in summer because the SST is higher in open water following solar warming. The differences can reach several tens of W m^{-2} on average.

Given the high subgrid-scale variability of oceanic heat fluxes with MCO#2, one may expect changes in the simulated ice thickness distribution (ITD). The average concentration in each category and the open water/lead fraction are presented in Fig. 13 for winter and summer months, in the areas delineated in Fig. 3 and for simulations REF and S2.50. The mean ice thickness in a given category differs much less between the two experiments than its concentration, and is hence not shown in the figure. Although the differences are qualitatively well explained by the heterogeneity of heat fluxes discussed above, it turns out that MCO has quantitatively little influence on the ITD. The concentration of thick categories tend to increase, at the expense of the thinner ones that undergo higher heat fluxes, but the changes are at most a few percent. Attempts to evaluate the modeled ITD against observations have shown errors up to 20 % for some ice classes (Barthélemy et al., 2016), i.e. much larger than the differences between the experiments analyzed here.

4.4. Discussion

The analysis of model results in the previous sections has shown their high sensitivity to the homogenization time scale be-

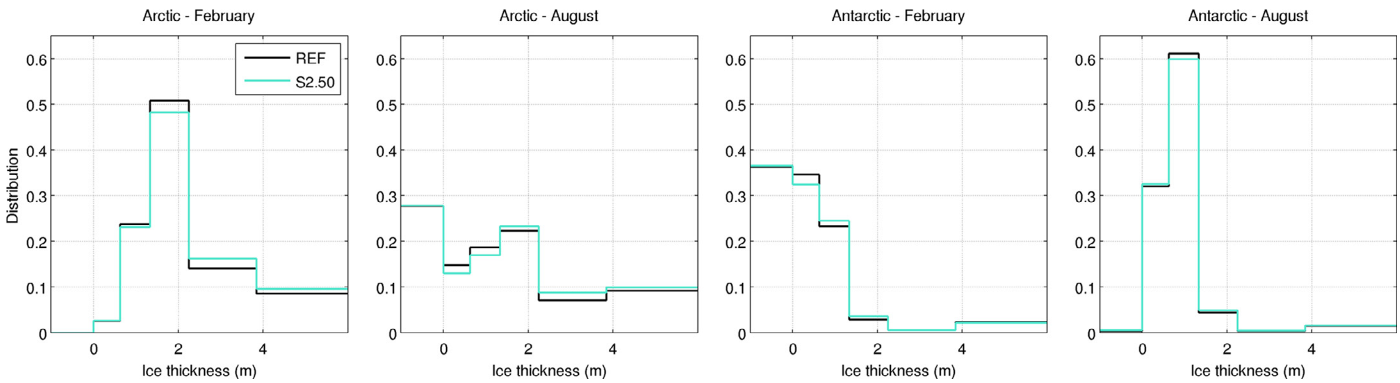

Fig. 13. Ice thickness distribution in experiments REF and S2.50, averaged in the areas depicted in Fig. 3 and where sea ice concentration exceeds 15 %, for February and August in the Arctic (left) and Antarctic (right). The value given for negative thicknesses represents the open water/lead fraction.

tween the columns. In MCO#1, in which complete homogenization takes place at each time step, i.e. every hour in our configuration, some effects exist at the subgrid scale but the model mean state is practically unchanged. This indicates that the heterogeneity in surface fluxes due to the presence of sea ice is not sufficient to induce, over one hour, very different oceanic regimes among the columns. A scheme like MCO#2 is therefore required to test the model sensitivity to a possible shift between the columns that grows over a longer period, corresponding to several time steps. Another strong motivation for MCO#2 is its ability to decouple the homogenization time scale from the model time step, in case MCO principles would have to be tested in different configurations.

Among the MCO#2 sensitivity experiments, it appears that impacts are relatively weak for homogenization time scales up to 10 h in our setup. Effects on the ocean and on the ice become substantial only for longer time scales. Typically, changes in the mean fields start to occur in winter when the convection reaches depths greater than the MLD in some of the columns. This process indeed allows waters from below, whose properties differ significantly from the surface, to be entrained within the mixed layer. While no convection occurs in summer, large-scale changes in sea ice emerge when the homogenization is sufficiently slow to let the solar radiation absorbed in open water be stored in the corresponding column, thereby delaying its influence on the ice melt.

Since quantitatively the MCO impact strongly depends on how fast the columns are homogenized, a physical estimation of the mixing time scale would be highly valuable. This is however a complex problem, which is beyond the scope of the present study. The mixing between columns is very likely variable in both space and time, depending first on their spatial distribution and second on the ocean and ice dynamics.

The column distribution is related to the size of ice floes of different thicknesses and how they are spread at the ocean surface. In a summer situation where small floes are evenly distributed among areas of open water, differences in water properties could be limited to a very thin layer close to the ice-ocean interface, while at greater depths, the large contact area between the columns would prevent distinct ocean regimes. By contrast, in a polynya in which sea ice is blown away from the coast by winds, there may exist a clear distinction between the ice-free portion of the area and the portion where thicker ice accumulates, allowing separate ocean columns to develop. The floe size distribution has long been recognized crucial for processes such as lateral melting (e.g., Steele, 1992). Its explicit modeling is nevertheless just starting to be considered for inclusion in large-scale operational forecast or climate models (Zhang et al., 2015; Horvat and Tziperman, 2015), which is promising for the current application. In the same vein, a representation of the lead width distribution could be important, as turbulent fluxes show a dependence on the size of leads (Marcq and Weiss, 2012).

The second factor that could influence the mixing of ocean columns is the ice-ocean relative velocities. If they are large, the heterogeneous surface fluxes are not continuously applied on the same fractions of the water column. For instance, a 300 m wide ice floe drifting at 10 cm s^{-1} needs less than one hour to be moved away from the region it was initially occupying and thus to cover another portion of the ocean surface. The model results indicate that such relative velocities are often encountered inside the Antarctic ice pack, while the ice drift tends to be slower in the Arctic (not shown). Besides, the ice motion induces vertical shear and turbulent mixing in the upper layers of the ocean (Morison et al., 1992; Smith and Morison, 1993; Kantha, 1995; Skyllingstad and Denbo, 2001), that tend to homogenize the oceanic columns quickly. Low relative velocities may thus be even more critical than the distribution of ice floes in allowing large differences between the columns.

Although the discussion presented above is only qualitative, we suspect that the homogenization time scale of 50 h used in experiment S2.50 might be a high value in most conditions. The effects that we have examined in more detail in that simulation must hence probably be considered as an upper limit for the impacts of a subgrid-scale representation of ice-ocean interactions. Experiment S2.250 should even more clearly be seen as an idealized test case.

A direct estimation of the homogenization time scale from observations would be extremely difficult to obtain. The required data would include repeated and simultaneous CTD profiles performed under different types of ice and in leads in a given area, in both the freezing and melting seasons, and for different ice-ocean relative velocity regimes. This would have to be compared to idealized, detailed processes studies in a model, in order to determine the horizontal mixing rate that gives the best agreement with observations. Parameter estimation based on data assimilation (e.g., Massonnet et al., 2014) might provide an alternative and help to guide the development of an empirical parameterization of the homogenization time scale, but the problem could be too loosely constrained for the method to be effective. Large eddy simulations of the sea ice-ocean system might be another approach to study the processes that modulate the horizontal mixing between the oceanic columns.

Other model features play a role in our estimation of MCO effects. In addition to the uncertainty on the mixing time scale, the open water fraction and the particular concentrations of ice of different thicknesses provided by the ITD display clear biases, that have a significant influence on the quantitative impact of MCO in our experiments. A short examination of the LIM results against IceBridge datasets (Kurtz et al., 2013) has actually demonstrated errors locally up to 20 % in the areal fractions of given ice categories. Compared to passive microwave satellite products, it also appears that the model underestimates the amount of leads in winter (Barthélemy et al., 2016).

A further issue regarding an accurate simulation of open water in summer is the lack of explicit lateral melt in LIM, whose adequate implementation is conditioned upon a representation of the ice floe size distribution (Steele, 1992). Although it is implicitly accounted for through melt of thin ice in the ITD (Bitz et al., 2001), it does not constitute a source of freshwater at the top of the ice-free column, as it should be. Yet, lateral melt during SHEBA represented up to 29 % of the total change in sea ice mass (Perovich et al., 2003). The absence of runoff from the snow and surface ice melt, or of a mechanism by which water originating from bottom melt could accumulate and subsequently be flushed laterally, might be a problem as well. Finally, Holland (2003) note that to achieve a realistic representation of summer warming and freshening of the open water surface, the latter must be embedded within the ice cover, in order to hinder direct lateral mixing between the lead and the under-ice ocean system. This is in line with the modeling results of Skyllingstad et al. (2005). However, it raises technical difficulties in a full three-dimensional model and has not been addressed here.

Although it requires substantial modifications in the model, the MCO scheme consists mostly in repeating several times the vertical mixing and tracer update computations that are already done in the reference code. Since the TKE and NPC schemes are time-consuming portions of the code, our developments significantly increase the model integration time. MCO#1 and MCO#2 are respectively 1.4 and 2.2 times more demanding in CPU time than the reference simulation. Optimization has not been a major concern so far, but it is clear that both versions could benefit from reducing the number of columns, possibly focusing on open water and thin and thick ice classes only. Reducing the amount of output fields in MCO#2 would be another straightforward source of performance improvement. Finally, the memory use is also larger with MCO#2 due to several additional three-dimensional fields that exist for all six columns (temperature, salinity, turbulent kinetic energy and turbulent mixing coefficients).

5. Conclusions

The sensitivity study presented in this paper intended to examine the effects of a representation of the heterogeneous nature of sea ice-ocean interactions in the global model NEMO-LIM. A multi-column ocean scheme has been developed, in which the subgrid-scale surface boundary conditions related to the ice thickness distribution present in LIM can be explicitly taken into account. While convection is always computed separately in open water and under the ice categories, whether distinct temperature and salinity profiles are allowed to be maintained over several time steps dictates if the model turbulent mixing scheme has to be called individually in each column as well. This distinction gives rise to two scheme versions that differ significantly in complexity. Nonetheless, model computations relative to ocean dynamics and lateral mixing are unmodified in both cases.

By using the actual buoyancy fluxes and column areas provided by the sea ice model, if lateral mixing occurs at each time step, there exist subgrid-scale effects in ocean convection but large-scale impacts on the model mean state are practically nonexistent. One option to artificially amplify the effect of subgrid-scale fluxes is to apply the salt rejections in a column of arbitrarily small extent as in Jin et al. (2015). We rather chose to maintain the columns over several time steps. By doing so, we obtained a number of physically plausible effects. The major ones are a reduction in mixed layer depths and an increase in sea ice extent and volume at the seasonal minimum, themselves explained by decreases in the oceanic heat flux at the ice base. Mean temperature and salinity profiles are only weakly affected. Nevertheless, in the Antarctic, changes of up to 0.15 °C are found at a few hundreds meters depth in the Ross and Weddell Seas and along the coast of East Antarctica, which are key areas for the formation of bottom waters. The length of our model runs is however too short to evaluate the long-term effects of the multi-column ocean scheme on these water masses. In the particular configuration used in our analysis, the scheme causes the model to underestimate mixed layer depths, mostly in the Antarctic, and reinforces the positive summer ice bias. The increase in Southern Hemisphere summer sea ice would actually be beneficial with other setups and forcing formulations, in which the Antarctic minimum extent is often too low (e.g., Rousset et al., 2015).

We noted that substantial effects on the ocean and sea ice start to appear when the time scale of homogenization between the columns is of the order or larger than 10 h. The large sensitivity to this time scale implies that additional work is required to estimate the lateral mixing rate from a strong physical basis, and thereby to reach a robust implementation of the multi-column ocean scheme and an precise quantitative evaluation of its impact. This is dependent on several other model features, among which an accurate representation of the ice thickness distribution and of the open water fraction, floe size distribution, lateral melting, runoff from the ice and embedment of leads within the sea ice cover. Those are all topics which deserve additional research and developments.

To fulfill the objective of this study, an advanced multi-column ocean scheme has been developed, making use of the full ice thickness distribution of LIM. This comprehensive scheme allows an in-depth examination of the role of subgrid-scale sea ice-ocean interactions. It would also be a highly valuable tool to assess their impacts in atmosphere-ice-ocean coupled simulations, or with models including a representation of the biogeochemistry (e.g., Long et al., 2015). This fully justifies the computational overhead associated with it. For other applications though, the first order effects could be captured using a simplified version of the scheme. The most important feature to include in a model is certainly the stark contrast between the open waters and the under-ice, which is much larger than between the different ice classes. Allowing the existence of separate upper ocean temperatures in summer for the ice-covered and open water fractions of grid cells, for a time scale longer than the model time step, appears to be the minimal requirement in terms of subgrid-scale sea ice-ocean interactions

Acknowledgments

We thank Ralph Timmermann and two anonymous reviewers for their valuable comments that contributed to improve this manuscript. We are also grateful to Martin Vancoppenolle, Julien Le Sommer and Eric Deleersnijder for their careful reading of the original text.

A. Barthélemy and H. Goosse are respectively Research Assistant and Research Director with the Fonds de la Recherche Scientifique (F.R.S.-FNRS/Belgium), which supports this work. G. Madec was also supported by EU-FP7 project SWARP under grant agreement 607476. Computational resources have been provided by the supercomputing facilities of the Université catholique de Louvain (CISM/UCL) and the Consortium des Equipements de Calcul Intensif en Fédération Wallonie Bruxelles (CECI) funded by the F.R.S.-FNRS under convention 2.5020.11.

References

Barthélemy, A., Fichefet, T., Goosse, H., Madec, G., 2015. Modeling the interplay between sea ice formation and the oceanic mixed layer: limitations of simple brine rejection parameterizations. Ocean Modell. 86, 141–152. doi:10.1016/j.ocemod.2014.12.009.

Barthélemy, A., Fichefet, T., Goosse, H., 2016. Spatial heterogeneity of ocean surface boundary conditions under sea ice. Ocean Modell. doi:10.1016/j.ocemod.2016.05.003.

Bitz, C.M., Holland, M.M., Weaver, A.J., Eby, M., 2001. Simulating the ice-thickness distribution in a coupled climate model. J. Geophys. Res. 106, 2441–2463. doi:10.1029/1999JC000113.

Blanke, B., Delecluse, P., 1993. Variability of the tropical Atlantic Ocean simulated by a general circulation model with two different mixed-layer physics. J. Phys. Oceanogr. 23, 1363–1388. doi:10.1175/1520-0485(1993)023⟨1363:VOTTAO⟩2.0.CO;2.

Close, S.E., Goosse, H., 2013. Entrainment-driven modulation of Southern Ocean mixed layer properties and sea ice variability in CMIP5 models. J. Geophys. Res. Oceans 118, 2811–2827. doi:10.1002/jgrc.20226.

Comiso, J.C., 2000. Bootstrap Sea Ice Concentrations from Nimbus-7 SMMR and DMSP SSM/i-SSMIS. Version 2. [1979-2012]. NASA National Snow and Ice Data Center Distributed Active Archive Center, Boulder, Colorado, USA doi:10.5067/J6JQLS9EJ5HU.

Conkright, M.E., Locarnini, R.A., Garcia, H.E., O'Brien, T.D., Boyer, T.P., Stephens, C., Antonov, J.I., 2002. World Ocean Atlas 2001, Digital Media. National Oceanographic Data Center., Silver Spring, Maryland, USA.

Couldrey, M.P., Jullion, L., Naveira Garabato, A.C., Rye, C., Herráiz Borreguero, L., Brown, P.J., Meredith, M.P., Speer, K.L., 2013. Remotely induced warming of Antarctic bottom water in the eastern Weddell gyre. Geophys. Res. Lett. 40, 2755–2760. doi:10.1002/grl.50526.

Fahrbach, E., Hoppema, M., Rohardt, G., Schröder, M., Wisotzki, A., 2004. Decadal-scale variations of water mass properties in the deep Weddell Sea. Ocean Dyn. 54, 77–91. doi:10.1007/s10236-003-0082-3.

Goosse, H., 1997. Modelling the large-scale behaviour of the coupled ocean-sea-ice system. Université catholique de Louvain. Ph.D. thesis..

Gordon, A.L., Huber, B.A., 1984. Thermohaline stratification below the Southern Ocean sea ice. J. Geophys. Res. 89, 641–648. doi:10.1029/JC089iC01p00641.

Hibler, W.D., 1980. Modeling a variable thickness sea ice cover. Mon. Wea. Rev. 108, 1943–1973. doi:10.1175/1520-0493(1980)108⟨1943:MAVTSI⟩2.0.CO;2.

Holland, M.M., 2003. An improved single-column model representation of ocean mixing associated with summertime leads: Results from a SHEBA case study. J. Geophys. Res. 108, 3107. doi:10.1029/2002JC001557.

Horvat, C., Tziperman, E., 2015. A prognostic model of the sea-ice floe size and thickness distribution. Cryosphere 9, 2119–2134. doi:10.5194/tc-9-2119-2015.

Ilıcak, M., Adcroft, A.J., Legg, S., 2014. A framework for parameterization of heterogeneous ocean convection. Ocean Modell. 82, 1–14. doi:10.1016/j.ocemod.2014.07.002.

Ilıcak, M., Drange, H., Wang, Q., Gerdes, R., Aksenov, Y., Bailey, D., Bentsen, M., Biastoch, A., Bozec, A., Böning, C., Cassou, C., Chassignet, E., Coward, A.C., Curry, B., Danabasoglu, G., Danilov, S., Fernandez, E., Fogli, P.G., Fujii, Y., Griffies, S.M., Iovino, D., Jahn, A., Jung, T., Large, W.G., Lee, C., Lique, C., Lu, J., Masina, S., George Nurser, A., Roth, C., Salas y Mélia, D., Samuels, B.L., Spence, P., Tsujino, H., Valcke, S., Voldoire, A., Wang, X., Yeager, S.G., 2016. An assessment of the Arctic Ocean in a suite of interannual CORE-II simulations. Part III: Hydrography and fluxes. Ocean Modell. 100, 141–161. doi:10.1016/j.ocemod.2016.02.004.

Jackson, J.M., Williams, W.J., Carmack, E.C., 2012. Winter sea-ice melt in the Canada Basin, Arctic Ocean. Geophys. Res. Lett. 39, L03603. doi:10.1029/2011GL050219.

Jin, M., Hutchings, J., Kawaguchi, Y., 2015. Sensitivity study of subgrid scale ocean mixing under sea ice using a two-column ocean grid in climate model CESM. Front. Earth Sci. 9, 594–604. doi:10.1007/s11707-014-0489-9.

Kalnay, E., Kanamitsu, M., Kistler, R., Collins, W., Deaven, D., Gandin, L., Iredell, M., Saha, S., White, G., Woollen, J., Zhu, Y., Leetmaa, A., Reynolds, R., Chelliah, M., Ebisuzaki, W., Higgins, W., Janowiak, J., Mo, K.C., Ropelewski, C., Wang, J., Jenne, R., Joseph, D., 1996. The NCEP/NCAR 40-Year Reanalysis Project. Bull. Amer. Meteor. Soc. 77, 437–471. doi:10.1175/1520-0477(1996)077⟨0437:TNYRP⟩2.0.CO;2.

Kantha, L.H., 1995. A numerical model of Arctic leads. J. Geophys. Res. 100, 4653–4672. doi:10.1029/94JC02348.

Krishfield, R., Toole, J., Proshutinsky, A., Timmermans, M.L., 2008. Automated ice-tethered profilers for seawater observations under pack ice in all seasons. J. Atmos. Oceanic Technol. 25, 2091–2105. doi:10.1175/2008JTECHO587.1.

Kurtz, N.T., Farrell, S.L., Studinger, M., Galin, N., Harbeck, J.P., Lindsay, R., Onana, V.D., Panzer, B., Sonntag, J.G., 2013. Sea ice thickness, freeboard, and snow depth products from Operation IceBridge airborne data. Cryosphere 7, 1035–1056. doi:10.5194/tc-7-1035-2013.

Leppäranta, M., Lensu, M., Kosloff, P., Veitch, B., 1995. The life story of a first-year sea ice ridge. Cold Reg. Sci. Technol. 23, 279–290. doi:10.1016/0165-232X(94)00019-T.

Long, M.C., Lindsay, K., Holland, M.M., 2015. Modeling photosynthesis in sea ice-covered waters. J. Adv. Model. Earth Syst. 7, 1189–1206. doi:10.1002/2015MS000436.

Losch, M., Herlufsen, S., Timmermann, R., 2006. Effects of heterogeneous surface boundary conditions on parameterized oceanic deep convection. Ocean Modell. 13, 156–165. doi:10.1016/j.ocemod.2005.12.003.

Madec, G., 2008. NEMO Ocean Engine. Note du Pôle de Modélisation, 27. Institut Pierre-Simon Laplace, France. ISSN No 1288-1619

Madec, G., Delecluse, P., Crepon, M., Chartier, M., 1991. A three-dimensional numerical study of deep-water formation in the Northwestern Mediterranean Sea. J. Phys. Oceanogr. 21, 1349–1371. doi:10.1175/1520-0485(1991)021⟨1349:ATDNSO⟩2.0.CO;2.

Marcq, S., Weiss, J., 2012. Influence of sea ice lead-width distribution on turbulent heat transfer between the ocean and the atmosphere. Cryosphere 6, 143–156. doi:10.5194/tc-6-143-2012.

Marshall, J., Plumb, R.A., 2007. Atmosphere, Ocean and Climate Dynamics, An Introductory Text. Volume 93 of International Geophysics Series. Academic Press.

Martinson, D.G., 1990. Evolution of the southern ocean winter mixed layer and sea ice: open ocean deepwater formation and ventilation. J. Geophys. Res. 95, 11641–11654. doi:10.1029/JC095iC07p11641.

Massonnet, F., Goosse, H., Fichefet, T., Counillon, F., 2014. Calibration of sea ice dynamic parameters in an ocean-sea ice model using an ensemble Kalman filter. J. Geophys. Res. Oceans 119, 4168–4184. doi:10.1002/2013JC009705.

Massonnet, F., Mathiot, P., Fichefet, T., Goosse, H., König Beatty, C., Vancoppenolle, M., Lavergne, T., 2013. A model reconstruction of the Antarctic sea ice thickness and changes over 1980–2008 using data assimilation. Ocean Modell. 64, 67–75. doi:10.1016/j.ocemod.2013.01.003.

Maykut, G.A., 1982. Large-scale heat exchange and ice production in the central Arctic. J. Geophys. Res. 87, 7971–7984. doi:10.1029/JC087iC10p07971.

Maykut, G.A., McPhee, M.G., 1995. Solar heating of the Arctic mixed layer. J. Geophys. Res. 100, 24691–24703. doi:10.1029/95JC02554.

Morison, J.H., McPhee, M.G., Curtin, T.B., Paulson, C.A., 1992. The oceanography of winter leads. J. Geophys. Res. 97, 11199–11218. doi:10.1029/92JC00684.

Nguyen, A.T., Menemenlis, D., Kwok, R., 2009. Improved modeling of the Arctic halocline with a subgrid-scale brine rejection parameterization. J. Geophys. Res. 114, C11014. doi:10.1029/2008JC005121.

Perovich, D.K., Grenfell, T.C., Richter-Menge, J.A., Light, B., Tucker, W.B., Eicken, H., 2003. Thin and thinner: Sea ice mass balance measurements during SHEBA. J. Geophys. Res. 108, 8050. doi:10.1029/2001JC001079.

Polyakov, I.V., Pnyushkov, A.V., Rember, R., Padman, L., Carmack, E.C., Jackson, J.M., 2013. Winter convection transports Atlantic water heat to the surface layer in the Eastern Arctic Ocean. J. Phys. Oceanogr. 43, 2142–2155. doi:10.1175/JPO-D-12-0169.1.

Roquet, F., Charrassin, J.B., Marchand, S., Boehme, L., Fedak, M., Reverdin, G., Guinet, C., 2011. Delayed-mode calibration of hydrographic data obtained from animal-borne satellite relay data loggers. J. Atmos. Oceanic Technol. 28, 787–801. doi:10.1175/2010JTECHO801.1.

Roquet, F., Wunsch, C., Forget, G., Heimbach, P., Guinet, C., Reverdin, G., Charrassin, J.B., Bailleul, F., Costa, D.P., Huckstadt, L.A., Goetz, K.T., Kovacs, K.M., Lydersen, C., Biuw, M., Nøst, O.A., Bornemann, H., Ploetz, J., Bester, M.N., McIntyre, T., Muelbert, M.C., Hindell, M.A., McMahon, C.R., Williams, G., Harcourt, R., Field, I.C., Chafik, L., Nicholls, K.W., Boehme, L., Fedak, M.A., 2013. Estimates of the Southern Ocean general circulation improved by animal-borne instruments. Geophys. Res. Lett. 40. doi:10.1002/2013GL058304. 2013GL058304

Rousset, C., Vancoppenolle, M., Madec, G., Fichefet, T., Flavoni, S., Barthélemy, A., Benshila, R., Chanut, J., Levy, C., Masson, S., Vivier, F., 2015. The Louvain-La-Neuve sea ice model LIM3.6: global and regional capabilities. Geosci. Model Dev. 8, 2991–3005. doi:10.5194/gmd-8-2991-2015.

Schmidtko, S., Johnson, G.C., Lyman, J.M., 2013. MIMOC: a global monthly isopycnal upper-ocean climatology with mixed layers. J. Geophys. Res. Oceans 118, 1658–1672. doi:10.1002/jgrc.20122.

Schweiger, A., Lindsay, R., Zhang, J., Steele, M., Stern, H., Kwok, R., 2011. Uncertainty in modeled Arctic sea ice. J. Geophys. Res. 116, C00D06. doi:10.1029/2011JC007084.

Shaw, W.J., Stanton, T.P., 2014. Vertical diffusivity of the Western Arctic Ocean halocline. J. Geophys. Res. Oceans 119, 5017–5038. doi:10.1002/2013JC009598.

Skyllingstad, E.D., Denbo, D.W., 2001. Turbulence beneath sea ice and leads: a coupled sea ice/large-eddy simulation study. J. Geophys. Res. 106, 2477–2497. doi:10.1029/1999JC000091.

Skyllingstad, E.D., Paulson, C.A., Pegau, W.S., 2005. Simulation of turbulent exchange processes in summertime leads. J. Geophys. Res. 110, C05021. doi:10.1029/2004JC002502.

Smith, D.C., Morison, J.H., 1993. A numerical study of haline convection beneath leads in sea ice. J. Geophys. Res. 98, 10069–10083. doi:10.1029/93JC00137.

Steele, M., 1992. Sea ice melting and floe geometry in a simple ice-ocean model. J. Geophys. Res. 97, 17729–17738. doi:10.1029/92JC01755.

Thorndike, A.S., Rothrock, D.A., Maykut, G.A., Colony, R., 1975. The thickness distribution of sea ice. J. Geophys. Res. 80, 4501–4513. doi:10.1029/JC080i033p04501.

Timmermans, M.L., 2015. The impact of stored solar heat on Arctic sea ice growth. Geophys. Res. Lett. 42, 6399–6406. doi:10.1002/2015GL064541.

Toole, J.M., Timmermans, M.L., Perovich, D.K., Krishfield, R.A., Proshutinsky, A., Richter-Menge, J.A., 2010. Influences of the ocean surface mixed layer and thermohaline stratification on Arctic Sea ice in the central Canada Basin. J. Geophys. Res. 115, C10018. doi:10.1029/2009JC005660.

Vancoppenolle, M., Fichefet, T., Goosse, H., Bouillon, S., Madec, G., Morales Maqueda, M.A., 2009. Simulating the mass balance and salinity of Arctic and Antarctic sea ice. 1. Model description and validation. Ocean Modell. 27, 33–53. doi:10.1016/j.ocemod.2008.10.005.

Wong, A.P.S., Riser, S.C., 2011. Profiling float observations of the upper Ocean under sea ice off the Wilkes Land Coast of Antarctica. J. Phys. Oceanogr. 41, 1102–1115. doi:10.1175/2011JPO4516.1.

Zhang, J., Schweiger, A., Steele, M., Stern, H., 2015. Sea ice floe size distribution in the marginal ice zone: theory and numerical experiments. J. Geophys. Res. Oceans 120, 3484–3498. doi:10.1002/2015JC010770.